ARTICLE

Precise Sub-Angstrom Ion Separation Using Conjugated Microporous Polymer Membranes

Zongyao Zhou, Dong Guo, Digambar B. Shinde, Li Cao, Zhen Li, Xiang Li, Dongwei Lu, and Zhiping Lai*

Cite This: *ACS Nano* 2021, 15, 11970−11980

Read Online

ACCESS | Metrics & More | Article Recommendations | SI Supporting Information

ABSTRACT: Polymer membranes typically possess a broad pore-size distribution that leads to much lower selectivity in ion separation when compared to membranes made of crystalline porous materials; however, they are highly desirable because of their easy processability and low cost. Herein, we demonstrate the fabrication of ion-sieving membranes based on a polycarbazole-type conjugated microporous polymer using an easy to scale-up electropolymerization strategy. The membranes exhibited high uniform sub-nanometer pores and a precisely tunable membrane thickness, yielding a high ion-sieving performance with a sub-1 Å size precision. Both experimental results and molecular simulations suggested that the impressive ion-sieving performance of the CMP membranes originates from their uniform and narrow pore-size distribution.

KEYWORDS: conjugated microporous polymer, membrane, ion sieving, electropolymerization, precise separation, carbon nanotube film
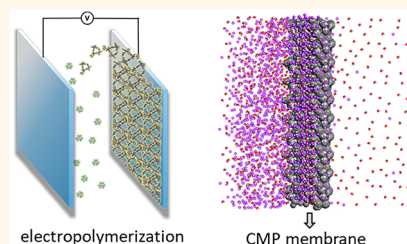
I on separation has wide applications in ion exchange, salinity energy conversion, chemical sensors, batteries, and seawater lithium mining.[1−3] A well-known example is the Na+/K+ channel in cell membranes, in which selective transport between Na+ and K+ regulates electrical potential across the membrane, which in turn plays a critical role in many biological activities.[4−6] The separation of ions is often challenging because of their similar sizes. It requires a high level of pore-size uniformity of the membranes.[7] Hence, most of the ion separations reported thus far were accomplished using membranes made of crystalline porous materials such as zeolites,[8−10] metal−organic frameworks (MOFs),[11−14] covalent organic frameworks (COFs),[15−17] and graphene oxide (GO).[18−22] However, these membranes are burdensome to prepare, difficult to scale-up, and expensive. In contrast, polymer membranes are much easier to fabricate, more stable, and cheaper. However, conventional polymer membranes have a broad pore-size distribution that leads to low selectivity.[23,24] Hence, designing polymer membranes with a uniform pore size is practically significant but technically challenging.

Recently, it has been reported that conjugated microporous polymers (CMPs) exhibit impressive pore-size uniformity and a high surface area.[25−27] The inherent rigidity of the conjugated structures renders them with a uniform permanent microporosity that facilitates gas storage and molecular sieving,[25] but it also results in a weak mechanical strength that precludes the usage of these polymers in pressure-driven membrane applications. Very recently, we developed a scalable electropolymerization (EP) strategy to fabricate CMP membranes with a carbon nanotubes (CNT) network to

enhance their mechanical strength by mimicking the skin-core architecture of spider silk and successfully applied these rigid CMP membranes for organic nanofiltration.[28] The prepared CMP membranes showed highly uniform pores of 1.08 nm and high surface area. However, achieving precise ion separation requires decreasing the pore size of CMP membranes down to sub-nanometer while maintaining their pore size homogeneity. Such a precise tailoring of pore architecture has rarely been achieved in polymer membranes. The porous structure of CMPs is largely determined by the monomer structure. The rich chemistry in the monomer design thus provides a rational approach to control the membrane structure on the molecular level.

In this study, we report the fabrication of ion-sieving membranes based on a conjugated microporous polymer prepared from 1,3,5-tris(N-carbazolyl) benzene (TCB) as the monomer. Our innovative strategy combines (1) the use of CMP to provide rigid sub-nanometer space inside the molecular structure so as to generate intrinsic micropores; (2) the well-designed electropolymerization strategy to facilitate the conjugated monomers generating only a well-defined dimer which benefits the uniformity of these
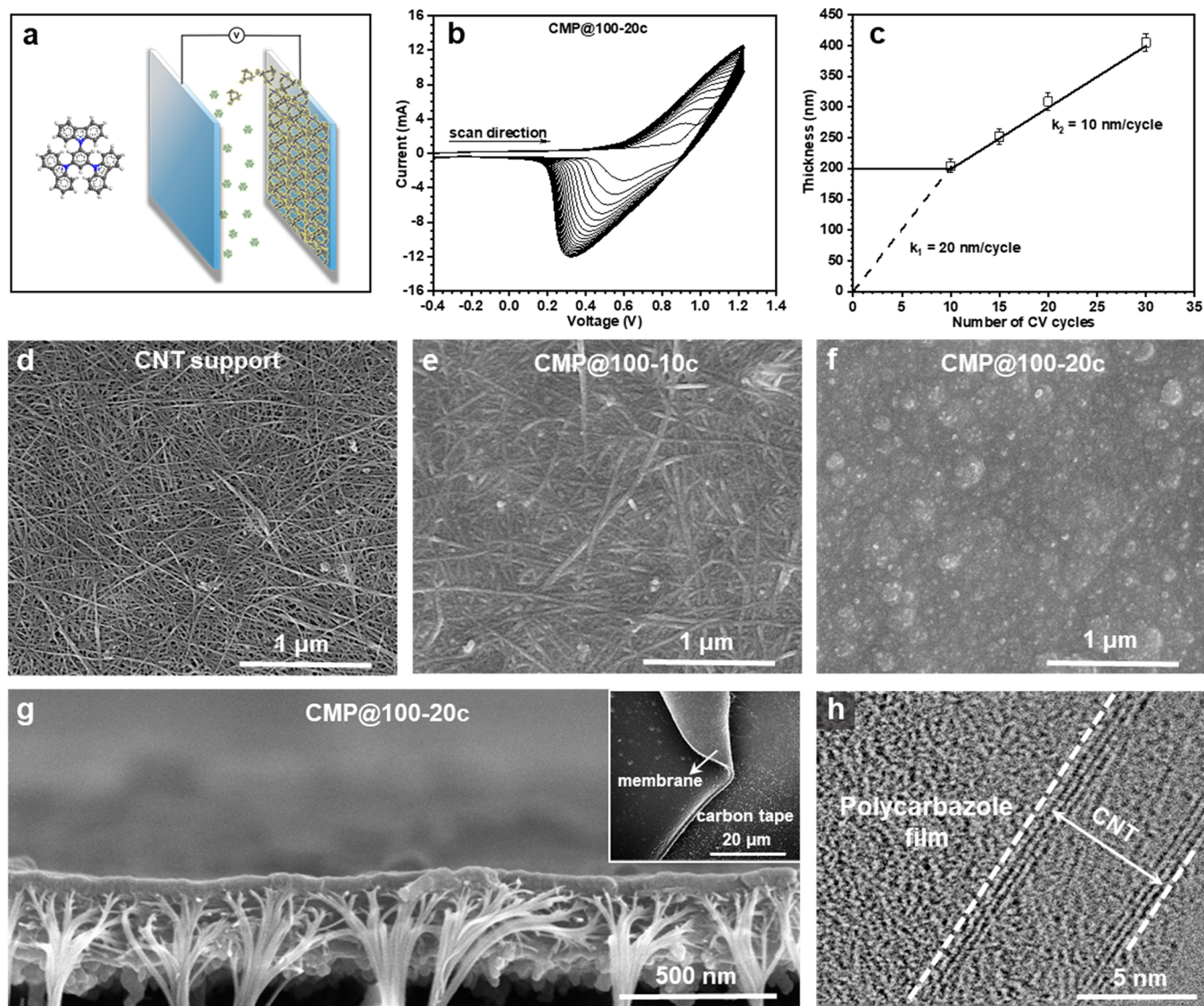
Figure 1. Membrane preparation and morphology. (a) Schematic illustration of the electropolymerization process. (b) CV profiles of the electropolymerization process recorded over 20 scan cycles. (c) Membrane thickness *vs* number of CV scans. (d) Surface SEM image of the CNT support. (e) Surface SEM image of CMP@100-10c. (f) Surface SEM image of CMP@100-20c. (g) Cross-sectional SEM image of CMP@100-20c. The inset SEM image shows the flexibility of the composite membrane. (h) TEM image of the polycarbazole attached tightly to CNT.

micropores; and (3) a precise control over membrane thickness at the nanometer scale to optimize the balance between fast ion transport and high ion selectivity. As a result, the prepared CMP membranes showed the capability to separate ions in sub-angstrom precision combined with fast ion transport. The performance is superior to that of the reported membranes fabricated by crystalline materials, such as MOFs, COFs, GO, and MXenes. Our innovative polymer membranes showed a great potential for applications in energy/environment-related ion separation processes.

RESULTS AND DISCUSSION

Because the sizes of most ions are smaller than 1 nm, hence 1,3,5-tris(*N*-carbazolyl) benzene (TCB) was selected in this study as the basic building block. Molecular simulations predicted that it could form a CMP polymer with a pore size of ∼0.85 nm (Figure S1). However, this carbazole structure is too rigid to form a robust membrane. Hence, using our earlier

strategy,[28] CMP membranes were synthesized in a CNT network through an electropolymerization process (Figure S2) to form compact composite membranes to enhance their mechanical strength. Polymerization was conducted in an electrochemical cell, as shown in Figure 1a. The CNT network (Figure 1d) was prepared through a simple vacuum-filtration method as described earlier.[28,29] The properties of the CNT support are presented in Figures S3 and S4. This CNT network possessed a number of desirable features, such as a smooth surface (Figure S3b) and high permeability (Figure S4f), mechanical strength, and conductivity.[28] The support was attached to a commercial hydrophilic polytetrafluoroethylene (PTFE) microfiltration membrane (0.2 μm pore size) to form a working electrode. CMP membranes were grown on the CNT supports by cyclic voltammetry (CV) scanning between −0.8 and 1.23 V (*vs* Ag/Ag$^+$). The corresponding CV curves were recorded, as shown in Figure 1b. In the first positive CV scan (Figure S5), an oxidative peak was observed at 0.87 V due
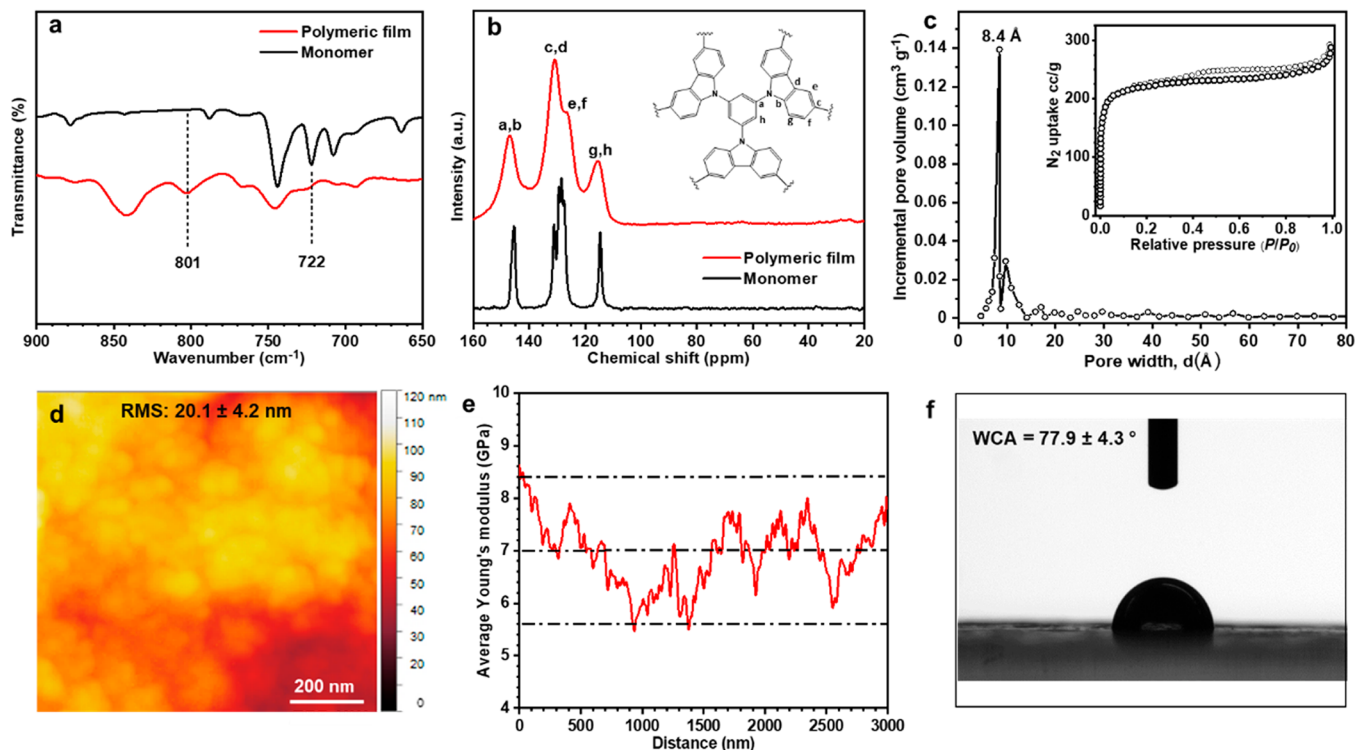
Figure 2. Membrane chemical and physical characterization. (a) FT-IR spectra of the monomer and polymeric film. (b) Solid-state ^{13}C NMR spectra of the monomer and polymeric film. (c) Nitrogen-physisorption isotherms and pore-size distribution of the polymeric film fabricated under 100 mV/s for 20 CV cycles. (d) AFM image of CMP@100-20c. (e) Young's modulus profile of CMP@100-20c. (f) Water contact angle image of CMP@100-20c.

to the oxidation of carbazoles to radicals. These radicals then coupled with each other to form dimeric carbazole (Figure S2), which is easily oxidized into cation radicals and quinoid dications.[30] In the negative CV scan, cations were reduced to the neutral state,[31] resulting in a reduction peak at 0.60 V. In the second and subsequent CV cycles, both the oxidation- and reduction-peak currents increased with an increase in the number of cycles, owing to continuous membrane growth.

The number of CV cycles and scanning rate are two important operation parameters to control membrane thickness. The membrane samples prepared at different numbers of CV cycles and scanning rates are denoted as CMP@X-Yc, where X is the scanning rate in mV/s and Y is the number of cycles. Figure 1c maps the membrane-growth rate at a scanning rate of 100 mV/s as a function of the number of cycles. In the first 10 cycles, the overall membrane thickness was similar to that of the CNT support (~200 nm). This indicates that membrane growth during this stage occurred inside the CNT support. This can also be observed in the scanning electron microscopy (SEM) and atomic force microscopy (AFM) images of CMP membranes in Figures 1e, S6, and S7, in which the CNT network was visible, but the gaps were completely filled. After 10 cycles, the membrane grew at a constant rate of 10 nm/cycle. Such precise control is very important to optimize the membrane thickness and thus the membrane performance. Dense and continuous membranes were formed after 20 (Figure 1f,g) and 30 cycles (Figure S8d,h). The membrane surface showed a granular structure, and surface roughness increased as the number of cycles increased. Because a rough surface may cause fouling, from the consideration of increasing membrane flux and reducing fouling, it is better to minimize the number of cycles. Figure

S9c shows that the average growth rate increased to 30 nm/ cycle when the scanning rate decreased to 10 mV/s. However, the membrane thus fabricated exhibited a loose structure inside the CNT network. Considering the requirements of membrane compactness and a precise control over membrane thickness, a high scanning rate is thus preferred. Figure 1g shows the cross section of the CMP@100-20c sample. It can be clearly seen that the polymer grew inside the CNT network as well as on its surface. The membrane at the surface was denser than that inside the network,[28] as suggested by the color contrast. It should be noted that the composite membrane was no longer brittle (Figure S10); as shown in the inset of Figure 1g, the membrane could be rolled without breaking. The composite structure was further analyzed by transmission electron microscopy (TEM) (Figure 1h), and it was found that the polymer was seamlessly attached to the CNT network with no gaps.

The chemical structure of the CMP membranes was evaluated by Fourier transform infrared (FT-IR) spectroscopy (Figure 2a) and solid-state ^{13}C nuclear magnetic resonance (^{13}C NMR) spectroscopy (Figure 2b). Compared with the FT-IR spectrum of the monomer, a new peak could be observed at 801 cm^{-1} in the spectrum of the CMP membrane, which is attributed to C-H vibrations in the trisubstituted carbazole rings of the polycarbazole chain, indicating the existence of dimeric carbazole.[32] The peak at 722 cm^{-1} is associated with C-H active sites in the carbazole units. The intensity of this peak reduced dramatically in the FT-IR spectrum of the CMP membrane, suggesting that almost all the redox sites participated in the polymerization reaction. The dimerization of carbazoles was also confirmed by the decrease in the intensities of the peaks at 126 ppm in the ^{13}C NMR spectra.
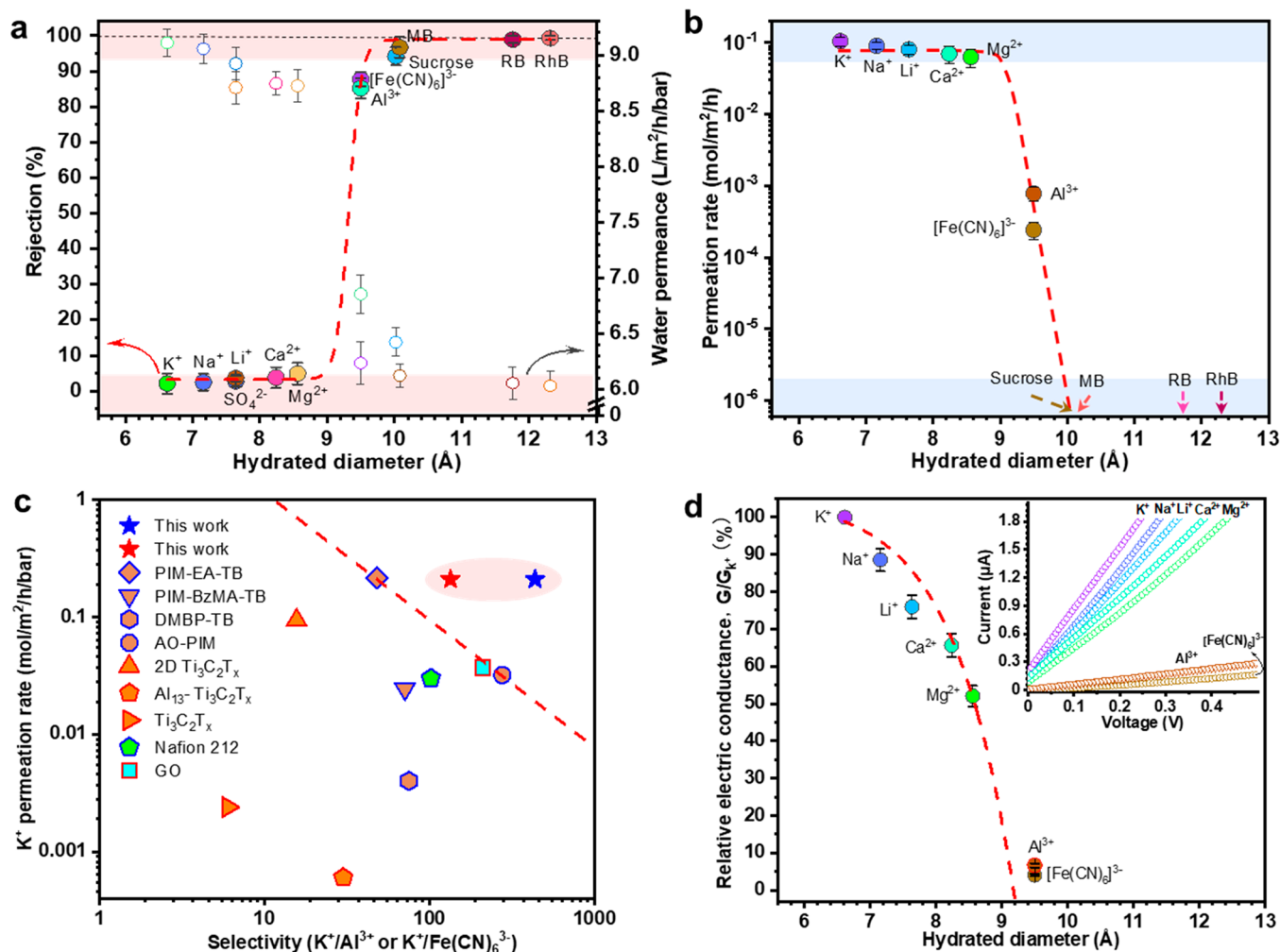
Figure 3. Ion-sieving performance of CMP@100-20c in various conditions. (a) Membrane performance in a pressure-driven process, illustrating the rejection of various solutes and the corresponding water permeance. (b) Membrane performance in a concentration-driven process. (c) K^+ permeation rate *vs* K^+/Al^{3+} (red edge) or $K^+/Fe(CN)_6^{3-}$ (blue edge) selectivity for CMP@100-20c membrane in the concentration-driven process. Typical ion separation data of state-of-the-art ion-sieving membranes such as polymers of intrinsic microporosity (PIMs), graphene-oxide (GO), carbides and/or nitrides of transition metals ($Ti_3C_2T_x$) membranes, and commercialized Nafion membrane that are reported in the literature[38-41] are included. (d) Ion-sieving performance monitored by current−voltage (I−V) measurements. Relative electric conductance is shown as a function of diameter of the solute. The inset shows current as a function of voltage.

Figure 2c shows the nitrogen-physisorption isotherm of the polycarbazole film fabricated under 100 mV/s for 20 cycles. A near-ideal Langmuir-type adsorption isotherm was obtained, which suggested a sharp pore-size distribution peaking at 8.4 Å and a high Brunauer−Emmett−Teller (BET) surface area of 809 m²/g. These pore-size distribution and surface-area values were similar to those of crystalline porous materials, such as COFs,[33] zeolite,[34,35] and MOFs.[36] The AFM image in Figure 2d shows that the surface roughness of CMP@100-20c is 20.1 ± 4.2 nm. Peak-force quantitative nanomechanical mapping (PFQNM) shows that the membrane exhibits an average Young's modulus of 7 GPa (Figures 2e and S11), which is almost 20 times higher than that of traditional polyamide membrane.[37] The water contact angle (WCA) of CMP@100-20c (Figure 2f) is 77.9 ± 4.3°, indicating its slightly hydrophilic nature.

Nine inorganic salts and four organic solutes of different sizes and charges (Table S1 and Figure S12c) were used to evaluate the ion-sieving performance of the membranes under pressure-driven, concentration-driven, and electrical-driven processes. In addition, the impacts of membrane thickness (number of CV cycles) on their water-permeance and ion-rejection properties were investigated (Figure S12a). Membrane selectivity initially increased with respect to the number of CV cycles (up to 20 cycles) and then became constant, indicating the formation of a defect-free membrane. Long-term filtration tests on the CMP@100-20c membrane suggest that its performance is stable (Figure S12b). Combining all these factors, the membranes prepared at a scanning rate of 100 mV/s for 20 cycles were deemed as the most optimal membrane structures for ion separation, and their performance will be discussed below.

The optimized CMP@100-20c membrane was first tested under pressure-driven operation. It is worth noting that many of the reported ion-separation studies were conducted using concentration-driven processes.[18,19,39,42] However, pressure-driven operation is of practical significance and is typically more challenging because it requires the membranes to be
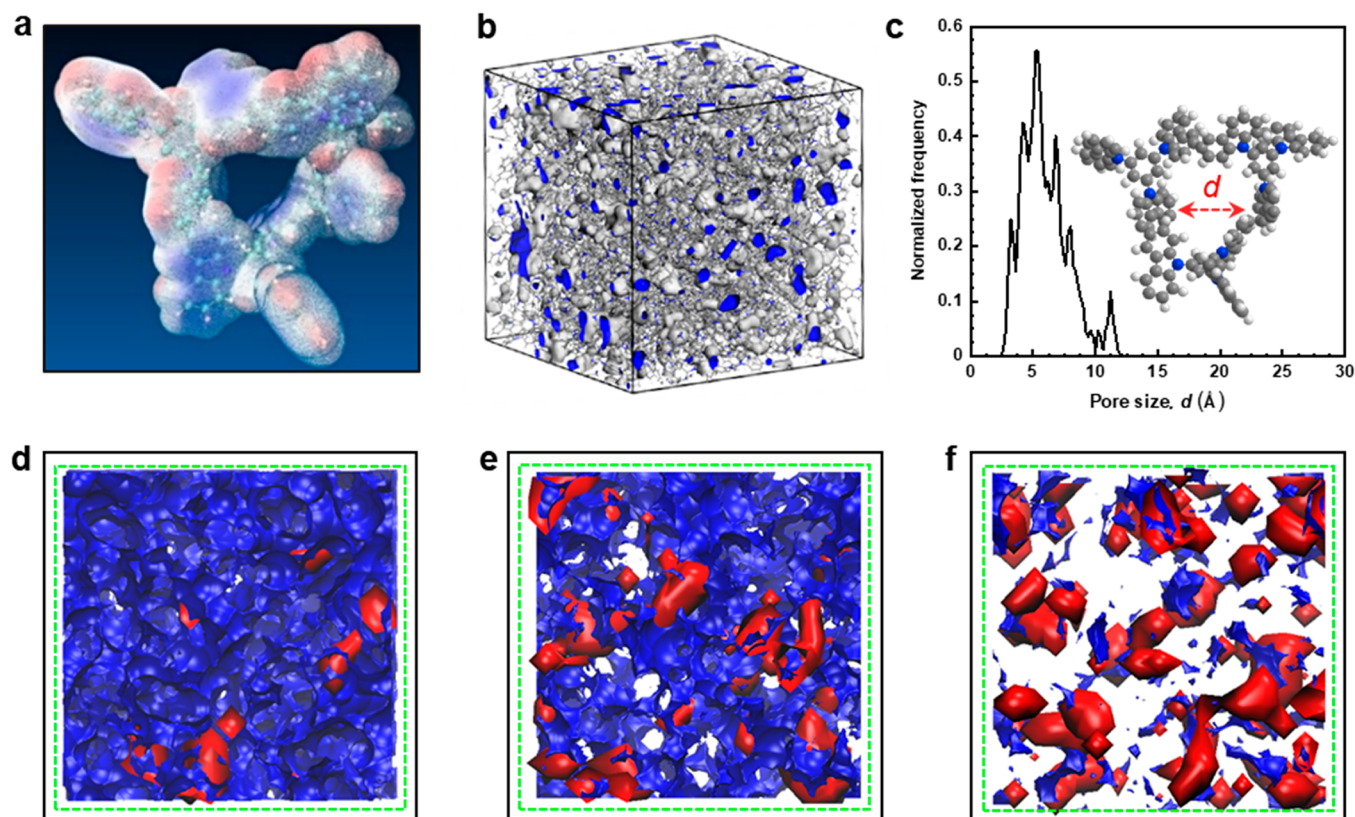
Figure 4. Simulated structure of the CMP membrane. (a) Pore size of the polymerized CMP membrane shown by electrostatic potentials on 0.001 au molecular surfaces. (b) Three-dimensional view of the CMP membrane (free volume in gray and Connolly surface in blue). (c) Simulated pore-size distribution, and the inset shows the pore structure. Interconnected (blue) and isolated (red) void space considering probes with diameters of (d) 4, (e) 6, and (f) 8 Å, respectively.

more robust. As shown in Figure 3a, the CMP@100-20c membrane showed a sharp rejection curve under pressure-driven operation. Specifically, the membrane showed a high ion permeation with hydrated diameters smaller than 9 Å and a high rejection of larger species. The rejection of the smallest ions (K^+) in this study was $2.1 \pm 2.9\%$. In the case of Mg^{2+} ions with a hydrated diameter of 8.56 Å, which is slightly larger than the pore size of the membrane (8.40 Å), the rejection was $4.9 \pm 3.1\%$. This is because the hydration shell could be partially distorted, flattened, or shredded before the ions entered the pores.[7,43] Hence, ions with a hydrated diameter slightly larger than the membrane-pore size can usually be transported through it. However, with $[Fe(CN)_6]^{3-}$ and Al^{3+}, membrane rejection increased dramatically to $87.7 \pm 2.0\%$ and $85.2 \pm 2.9\%$, respectively; it is worth noting that these ions have a similar hydrated size of 9.50 Å but opposite charges. Nevertheless, their close rejection values imply that the membrane-rejection mechanism was based on size sieving.

Analogous to the molecular weight cutoff (MWCO)[28,33] and molecular weight retention onset (MWRO),[28] hydrated diameter cutoff (HDCO), which is associated with 90% rejection, and hydrated diameter retention onset (HDRO), which is associated with 10% rejection, were defined to demonstrate the ion-sieving performance of the CMP@100-20c membrane. The HDCO and HDRO of the CMP@100-20c membrane were ∼9.50 and 9.0 Å, respectively. The narrow region between HDCO and HDRO indicates the excellent ion sieving. Membrane rejection values for big molecules such as sucrose (10.02 Å), methylene blue (MB, 10.08 Å), rose bengal (RB, 11.76 Å), and rhodamine B (RhB, 12.32 Å) were

calculated to be higher than 94%. The selectivity of the membrane with respect to salt/dye systems is illustrated in Figure S13. The membrane exhibited an excellent selectivity of ∼140 with respect to Na^+/RhB and 135.9 ± 4.1 with respect to Mg^{2+}/RhB, which is greater than the highest reported salt/dye selectivity of 120.[44]

To elucidate the ion-sieving mechanism, membrane-adsorption tests were conducted with both positive and negative solutes (Figures S14−S16). The adsorption capacity of our CMP membrane to $[Fe(CN)_6]^{3-}$ in the test is 3.18×10^{-2} (g/g), and the adsorption capacity to Al^{3+} is 2.31×10^{-6} (g/g). Such a small adsorption capacity ensured that the membrane reached the steady state within 10 min and excluded the adsorption effect. Furthermore, the separation mechanism was not based on the charge effect because of the following reasons. First, Figure S17 shows that the membrane surface charge was nearly neutral (2.4 to −4.3 mV) in the pH range of 6−7.2. Second, the membrane exhibited similar rejection values for both positive and negative ions with the same hydrated diameter, not only for the $[Fe(CN)_6]^{3-}$ and Al^{3+} pair as discussed earlier but also with SO_4^{2-} and Li^+ (Figure S12c). Third, the membrane exhibited a high rejection (>90%) with respect to electroneutral species such as sucrose, owing to their larger size when compared to membrane pores.

Concentration-driven tests were performed using a U-shaped glass filter.[18,19] An online recording system was used for these tests, and 1440 data points (1 point/min) were recorded for each ion solution. The rate of diffusion across the membrane was observed to be nearly constant for each salt over the experimental duration of 1440 min (Figure S18b).
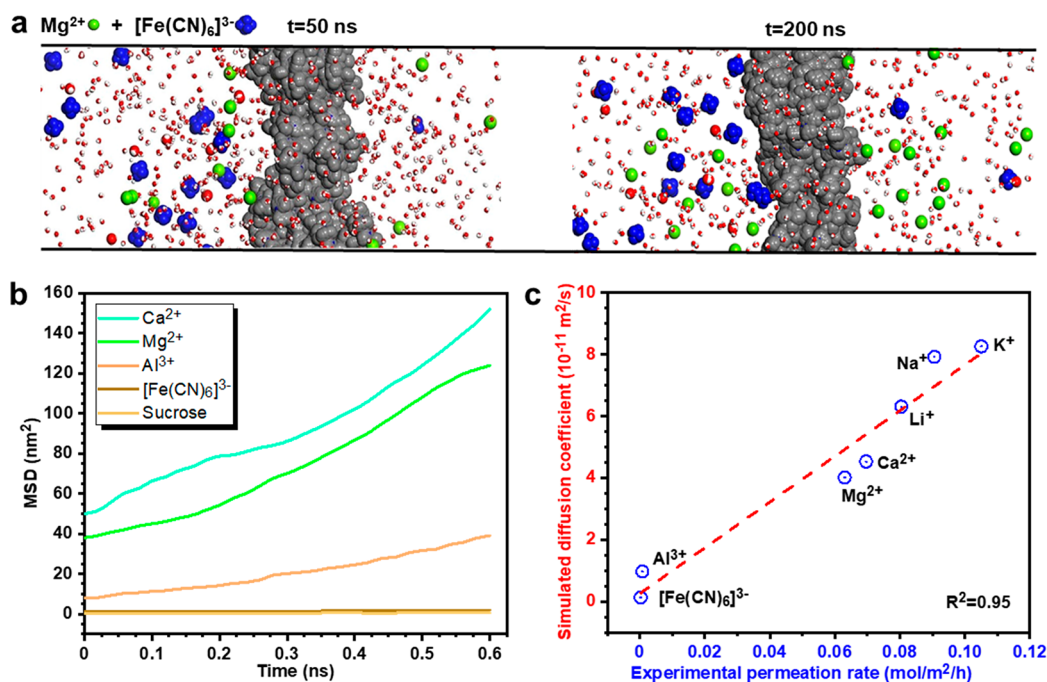
Figure 5. Molecular dynamics simulations and transport measurements. (a) Simulation snapshots at 50 and 200 ns for the 2-component mixed-ion diffusion system. Mg^{2+} and $[Fe(CN)_6]^{3-}$ ions are represented in green and blue, respectively. (b) Mean-squared displacement (MSD) of various ions through the membrane. (c) Simulated diffusion coefficients *vs* experimental permeation rates for different ions. The red dashed line is a linear fit to the data (blue circles).

The slopes of the recorded curves yielded permeation rates, as summarized in Figure 3b. K^+ showed the highest permeation rate of 0.105 mol/m²/h. Ion permeation followed the order of $K^+ > Na^+ > Li^+ > Ca^{2+} > Mg^{2+}$, which is consistent with the order of their hydrated ionic sizes. It should be noted that the ion transport rate of the membrane is very high in consideration of the low concentration of the feed solution (10 mmol/L salt solution), thus the low driving force (~0.5 bar osmotic pressure gradient). By normalizing the osmotic pressure, the permeation rate of K^+ was 0.21 mol/m²/h/bar, which is higher than that reported for Mxene membranes (0.19 mol/m²/h/bar),[39] GO membranes (0.08 mol/m²/h/bar),[18] physically confined GO membranes (2.63 × 10⁻⁴ mol/m²/h/bar),[19] and NF-270 (0.09 mol/m²/h/bar).[45] The ion selectivity of the membrane is also impressive (Figure 3c). The selectivity performance of the CMP@100-20c membrane surpasses those of existing intrinsic microporosity (PIMs), graphene-oxide (GO), carbides and/or nitrides of transition metals ($Ti_3C_2T_x$) membranes, commercialized Nafion 212 membrane,[38−41] and Nafion 211 membrane (Figure S19). The selectivity of K^+/Al^{3+} was 134, $K^+/[Fe(CN)_6]^{3-}$ was 436, and $Mg^{2+}/[Fe(CN)_6]^{3-}$ was 261. Larger molecules, including sucrose, MB, RB, and RhB, could not permeate through the membrane in the concentration-driven mode, even after 2 weeks.

The ion-sieving performance of the membrane was also tested by electrical measurements as sensitive current measurement enables a high-resolution detection. Current, as a function of voltage, was recorded and is shown in Figures S20 and 3d (inset). In the free state, when there was no membrane, Al^{3+} and $[Fe(CN)_6]^{3-}$ exhibited higher currents because of their higher electric charges. However, when a CMP@100-20c membrane was mounted between the two chambers of the cell (Figure S20b), the relative trend changed drastically. In this case, the current trend followed the order of $I_{K^+} > I_{Na^+} > I_{Li^+} > I_{Ca^{2+}} > I_{Mg^{2+}} \gg I_{Al^{3+}} \approx I_{[Fe(CN)_6]^{3-}}$, which is consistent with their hydrated ionic sizes. The currents obtained with Al^{3+} and $[Fe(CN)_6]^{3-}$ were very low, indicating that the membrane exhibited a high rejection of Al^{3+} and $[Fe(CN)_6]^{3-}$. Meanwhile, the current observed with the Mg^{2+} solution was 0.446 μA at 0.1 V, which is more than 20 times higher than that observed using $[Fe(CN)_6]^{3-}$. The slopes of the I−V curves yielded electric conductance, G. Figure 3d plots the relative changes in electric conductance with respect to solvent radius. The changes were normalized to the relative value of the electric conductance obtained using the K^+ solution (G_0). The relative electric conductance of Mg^{2+} was 52.0%, whereas that observed with $[Fe(CN)_6]^{3-}$ was 4.1%. As the difference in the hydrated ionic sizes of Mg^{2+} and $[Fe(CN)_6]^{3-}$ was 0.94 Å, it can hence be stated that the CMP membrane is capable of ion sieving at a sub-angstrom precision.

To support our proposed mechanism and to better understand the structures of polycarbazole membranes with highly uniform sub-nanometer pores, a structural model was generated and its properties were analyzed using the Multiwfn program.[46] The CMP monomer used in this study has a spiro center, and these monomers, upon cross-linking, pile up and form a 3D conjugated network, leading to intrinsic sub-nanometer spaces inside the molecular structure, as illustrated in Figure 4a. The gray areas in Figure 4b indicate a large fraction of free volume in the CMP membrane, which is consistent with the calculated high BET surface area. The pores of the membrane in the simulation show a very sharp distribution characterized by Zeo++ code,[47] as shown in Figure 4c, which confirms the experimental results obtained by nitrogen physisorption. The well-defined structure and highly uniform pores benefit from the homogeneous elementary pore

structure of dimeric carbazole, which is the only reaction product during the electropolymerization process.[48−50] Figure 4d−f shows the occurrence of continuous voids with respect to a series of probes with diameters of 4, 6, and 8 Å, respectively. When the smallest probe with a diameter of 4 Å was inserted, the voids were significantly interconnected and the membrane showed high porosity. As the probe size increased by 2 Å, the fraction of interconnected voids notably decreased, indicating the excellent sieving sensitivity of the membrane. When a theoretical probe with a diameter of 8 Å was used, the interconnected voids further decreased and the nonvoid areas or disconnected voids became dominant, suggesting that the ions/molecules with sizes larger than 8 Å could not permeate easily through the membrane. This result also indicated that most of the voids/pores with a large size were most likely to be disconnected. Therefore, although there were a fraction of large pores in the membrane, they contributed less to the diffusion of ions/molecules of this size. Nevertheless, these large pores are still not conducive to membrane selectivity.

To further understand the ion-sieving mechanism and the origin of the high performance observed in the membrane, molecular simulations were conducted with various ions and molecules. First, a 2-component mixed-ion diffusion system of $[Fe(CN)_6]^{3-}$ and Mg^{2+} was simulated and used to evaluate the ion-sieving performance (Figure 5a). It can be seen that Mg^{2+} and $[Fe(CN)_6]^{3-}$ were constantly moving in the system and exhibited vibrations of small amplitudes in most cases. The ions could jump from one free-volume hole to another hole only at appropriate times and positions, indicating that the size and distribution of free volume in the membrane had a significant influence on ion diffusion. At the beginning of the simulation, only water molecules were present in the permeate side of the CMP membrane along the z-direction in the system. At 200 ns, numerous Mg^{2+} ions (but only few $[Fe(CN)_6]^{3-}$ ions) could be found on the permeate side. This indicates that the diffusion of Mg^{2+} through the membrane was much faster than that of $[Fe(CN)_6]^{3-}$. This simulation result was consistent with the experimental results. We further evaluated the ion-permeation rate of the CMP membrane in terms of the mean-squared displacement (MSD). As shown in Figure 5b, MSD decreased with an increase in ionic or molecular size in the order of $MSD_{Ca^{2+}} > MSD_{Mg^{2+}} \gg MSD_{Al^{3+}} > MSD_{[Fe(CN)_6]^{3-}} \approx MSD_{sucrose}$. The simulated diffusion coefficients of K^+, Mg^{2+}, Al^{3+}, and $[Fe(CN)_6]^{3-}$ were 8.26×10^{-11}, 4.21×10^{-11}, 9.7×10^{-12}, and 1.3×10^{-12} m^2/s, respectively. As shown in Figure 5c, the simulated diffusivity of different ions through the membrane showed the same trend as the experimental results, with a good fitting value R^2 of 0.95.

Overall, we demonstrated an easily scaled-up electropolymerization process to synthesize CMP membranes for ion separation. The composite structures fabricated with the CMP matrix and a CNT network resulted in a high ductility and mechanical strength, which enabled the application of these membranes in pressure-driven ion-separation processes. In particular, due to their permanent intrinsic conjugated network structures, the CMP membranes exhibited excellent uniform sub-nanometer pores, which endowed the membrane with high ion-sieving performance. The sieving accuracy of the membrane was sub-1 Å in pressure-driven operations, which is the most precise value reported thus far for solute-solute separation using polymer membranes. Meanwhile, the ion-permeation rate of the CMP membrane was much higher than

that of most of the state-of-the-art membranes based on advanced materials such as MXene and GO. Both experimental and simulated results suggest that the impressive ion-sieving performance of the CMP membranes originates from their uniform and narrow pore-size distribution.

CONCLUSIONS

The concept of using CMPs to prepare membranes with conjugated micropores by an electropolymerization strategy has resulted in the generation of high performance ion-sieving membranes. The prepared polycarbazole CMP membranes exhibited a narrow pore-size distribution peaking at 8.4 Å and a high BET surface area of 809 m^2/g. The uniformity of the sub-nanometer pores and the surface area are comparable and, in some cases, superior to those of crystalline porous materials, such as COFs, zeolites, and MOFs. Unlike the membranes made of crystalline framework materials or delaminated 2D nanosheets that contain grain boundaries, the CMP membrane is structurally continuous and defect-free. Also, the CMP membrane does not require either thermal treatment or solvent exchange to activate the pores, as does many other porous membranes, which is also a critical issue that may induce defects. Besides, the formation of the CMP and the deposition of the membrane are simultaneously completed during the electropolymerization process, avoiding the secondary processing of CMP membranes. Importantly, CMPs as an important category of polymer materials whose rich monomer chemistry combined with the incorporation of tailored electropolymerization parameters and postsynthetic modification can provide great opportunities for rational control of the membrane structure at the molecular level.

METHODS

Materials. Carbon nanotubes powder (100 mg, length 5−30 μm, purity > 95%) was obtained from XFNANO, China. Tetrabutylammonium hexafluorophosphate (TBAPF$_6$, 99%) was purchased from Sigma-Aldrich and recrystallized twice in ethanol and vacuum-dried for 24 h before further use. All other chemicals were purchased from Sigma-Aldrich and used as received.

Preparation of CNT Supports. CNT powder and 1 g of sodium dodecylbenzenesulfonate were sonicated in 1000 mL of deionized water for 1.5 h using a probe ultrasonicator with a 25 mm probe at 360 W. The mixture was then centrifuged at 15 000 rpm for 40 min to remove any undispersed CNT powder. The collected supernatant was filtered under vacuum conditions onto a commercial hydrophilic polytetrafluoroethylene microfiltration membrane or a commercial anodic aluminum oxide membrane.

Fabrication of CMP Membranes. TCB was used to synthesize CMP membranes via an electropolymerization process. The polymerization conditions were precisely designed to obtain CMP membranes with smooth surfaces and relatively hydrophilic characteristics. Specifically, 32 mg of TCB and 1.55 g of TBAPF$_6$ were dissolved in 40 mL of a mixture of anhydrous CH_2Cl_2 and CH_3CN (3/2, v/v) by stirring for 1 h to obtain a homogeneous electrolyte solution. The solution was then loaded in a standard three-electrode electrochemical cell attached to an electrochemical workstation (CH Instruments Inc., model 660C). A Ag/Ag$^+$ nonaqueous electrode was used as the reference electrode while the dried CNT support on a PTFE microfiltration membrane or a commercial anodic aluminum oxide membrane was used as the working electrode and a 4×6 cm^2 titanium metal plate was used as the counter electrode. CV was conducted in the range of −0.8 to 1.23 V at a predefined scanning rate. The synthesized membranes were immersed in a CH_2Cl_2 and CH_3CN mixture overnight to completely remove any unreacted monomers and electrolytes. Finally, the membranes were stored in deionized water until further use.

Characterization. A drop-shape analyzer (Kruss, DSA100, Germany) was employed to measure the water contact angle (WCA) of the membranes. The drop volume was set at 2.0 μL, and a nanosize and zeta potential analyzer (Litesizer 500, Anton Paar, Austria) was used to measure the zeta potential of the CNT suspension. The zeta potential of the membrane surface was measured using a solid-surface zeta-potential analyzer (Anton Paar GmbH, SurPASS 3, Austria). A capillary-flow porometer (Porolux 1000, IB-FT GmbH Berlin, Germany) was used to measure the pore size of the CNT support. The chemical state of the CNTs was analyzed by X-ray photoelectron spectroscopy (XPS, K-alpha, Thermo Fisher, USA) and Raman spectroscopy (XploRA PLUS, Horiba, Japan) in the wavelength range of 500−3000 cm^{-1}. An FEI Magellan 400 microscope and FEI Titan transmission electron microscope were used for SEM and high-resolution TEM analysis of the membranes, respectively. Membrane-surface roughness and surface Young's modulus were analyzed by AFM (Bruker Dimension Icon, Germany) with a PFQNM function. FT-IR (Thermo Fisher Scientific, Nicolet iS10, USA) and solid-state ^{13}C NMR (Bruker 500 MHz, Germany) were conducted to characterize the chemical properties of the membranes. Nitrogen-physisorption experiments were conducted at 77 K on a volumetric adsorption analyzer (Micromeritics ASAP 2420, USA) to evaluate membrane porosity; prior to measurement, the samples were evacuated at 393 K for 24 h.

Sieving Performance in a Pressure-Driven Process. Pressure-driven ion- and molecular-sieving tests were performed at room temperature (22 °C) using a homemade cross-flow test system (Figure S21), which was connected to a solution tank (2.5 L) to ensure that concentration changes in the feed side during the permeation test were negligible. The pressure on the feed side was set to 10 bar, and the permeate side was open to the atmosphere. A series of dye and inorganic salt solutions with concentrations of 100 and 1000 ppm were used as the feed solutions, respectively. The permeate in the steady state was collected, and its weight was monitored using a digital balance. Salt concentration was measured and calculated using a conductivity meter (CON2700, Eutech, USA) attached to an online PC system. Dye concentrations were measured using a UV−vis spectrophotometer (Agilent, Cary 5000, USA). The concentration of organic solutes was measured using a total organic carbon analyzer (TOC, Shimadzu, Japan). Finally, permeance P (L/m^2/h/bar) was calculated using eq 1

$$P = V/(A \cdot \Delta t \cdot \Delta P) \tag{1}$$

where V (L) is the volume of the permeated water collected during a certain time period Δt (h) at a pressure difference ΔP (bar) and A is the area of the membrane (m^2).

Solute rejection R (%) was calculated using eq 2

$$R\ (\%) = (1 - C_P/C_F) \times 100 \tag{2}$$

where C_P and C_F represent solute concentrations in the permeate and feed solutions, respectively.

The selectivity of solute A over solute B, α, was calculated using eq 3

$$\alpha = \frac{1 - R_A}{1 - R_B} \tag{3}$$

where R_A and R_B are the rejections of solutes A and B, respectively.

Sieving Performance in a Concentration-Driven Process. Concentration-driven sieving tests were conducted using a U-shaped glass filter. A 4 cm^2 membrane was fixed at the joint between the two filter chambers. The two chambers were filled with 250 mL of deionized water and 250 mL of salt solution (10 mmol/L) or dye solution (100 ppm), respectively. Samples were sourced at regular intervals for 24 h. Magnetic stirring was conducted in both chambers to avoid concentration-induced polarization. The ion-permeation rate was measured and calculated using a conductivity meter (CON2700, Eutech, USA) attached to an online PC system. To analyze organic solutes, a total organic carbon (TOC, Shimadzu, Japan) analyzer and a UV−vis spectrophotometer (Agilent, Cary 5000, USA) were

employed. The ion/molecular-permeation rate, J (mol/m^2/h), was calculated using eq 4

$$J = C \cdot V/(A \cdot \Delta t) \tag{4}$$

where C (mol/L) is the concentration on the permeate side, V (L) is the volume of the permeate solution, A is the membrane area (m^2), and Δt (h) is the test time.

Monitoring Sieving Performance by I−V Measurements. Electrical measurements were performed on an electrochemical workstation (CH Instruments Inc., model 660C) with a homemade electrochemical cell. The membrane was mounted between the two chambers of the cell, each of which contained a 10 mmol/L salt solution; furthermore, a pair of Ag/AgCl electrodes was positioned into the chambers. Ionic conductance was measured in the voltage range of −0.5 to 0.5 V at a step size of 0.05 V/s, and current was recorded as a function of the applied voltage. Relative electric conductance, G/G_{K^+}, was calculated using eq 5

$$\frac{G}{G_{K^+}} = \frac{I/U}{I_{K^+}/U_{K^+}} \tag{5}$$

where G (S), I (A), and U (V) represent electrical conductance, current, and potential, respectively. G_{K^+}, I_{K^+}, and U_{K^+} are the electrical conductance, current, and potential, respectively, obtained during K$^+$ ion diffusion.

Adsorption Tests. A homemade setup (Figure S14) connected to an online data-recording system was used to test membrane adsorption. A glass bottle was filled with 250 mL of the ion solution; the CMP@100-20c membrane (4 cm^2) was also placed in this bottle, which was then capped. The solution volume and membrane size were similar to those used in ion-diffusion tests. The solution was stirred to ensure homogeneity, and its concentration was monitored by a conductivity meter (CON2700, Eutech, USA). Tests were conducted on each sample for 3 days (4500 min) to ensure adsorption equilibrium. The adsorption capacity (AC) of the test membrane was later calculated using eq 6

$$AC = \frac{(C_i - C_f) \times V}{W_m} \tag{6}$$

where C_i (g/L) and C_f (g/L) are ion concentrations before and after the adsorption experiments, respectively, V (L) is the volume of the solution, and W_m (g) is the weight of the membrane.

Quantum Chemical Calculations. The optimized structures and their electronic wave functions were evaluated using the Gaussian 09 package.[51] The TCB monomer and structural unit (Figure 4a) of the membrane were optimized using the M06-2X method with a compound basis set. The H element and non-bridgehead C and N atoms used the 6-31G(d) basis set, and the 6-311+G(d) basis set was employed for all bridgehead C and N atoms. Single-point frequency calculations were carried out to ensure that the final structures contained no imaginary frequency. To determine the pore size of the membrane, electrostatic potentials on the 0.001 au molecular surfaces[52] of the structural unit were computed based on Multiwfn programs[46] using the optimized geometries.

Construction of Atomic Models. All molecular dynamics calculations were performed on the Materials Studio (MS) program. In this study, the number (n) of membranes was set to 48 and the end groups were saturated by H atoms. First, an aggregation with six layers of membrane models was selected to build the membrane using amorphous cell modules. Second, during the 40-cycle annealing process, a 2.0 ns molecular dynamics simulation at 600 K was performed in the constant-temperature, constant-volume (NVT) ensemble with the COMPASS force field. Subsequently, the temperature was gradually reduced to 300 K within 2.0 ns. Then, the simulation system was relaxed by constant-temperature, constant-pressure (NPT) simulations (300 K and 1.0 atm). During annealing, the number of H$_2$O molecules added in each cycle was monitored to estimate the equilibrium state, and it was found that the number of H$_2$O molecules became nearly a constant at ~37 cycles, suggesting

sufficient pretreatment of the membrane with H_2O. Finally, to further relax the membrane, a 10 ns molecular dynamics simulation was performed at 300 K after 40-cycle annealing to realize a stable membrane structure. This structure was used to construct a histogram of N⋯N distances between two adjacent TCB moieties. Along the trajectory, membrane structures calculated after every 300 ps were extracted and 10 structures were selected. Among these, N⋯N distances corresponding to a value of 1440 (*i.e.*, $48 \times 3 \times 10$) were counted and a histogram was built. According to the histogram, the pore size was determined by the probability of N⋯N distances. The free volume of the above-constructed membrane system was simulated using the atomic volume and surface. In addition, an amorphous TCB unit ($\sim6 \times 6 \times 6$ nm^3) with a density of 1.39 g/cm^3, which is close to the experimental value, was built to analyze pore-size distribution using Zeo++.[47] These calculations were performed using GROMACS 4.6.7, GROMOS force field, and PRODRG modules.[53−55]

Simulation of Diffusion Coefficients. A visualizer module was used to establish H_2O molecules and K^+, Li^+, Na^+, Ca^{2+}, Mg^{2+}, and $[Fe(CN)_6]^{3-}$ while an amorphous cell module was used to establish the lattice of the membrane with H_2O and the listed ions. The lattice temperature was set at 298 K, and a periodic-boundary condition was used to ensure a constant concentration in the entire system throughout the simulation process. From the periodic-boundary conditions of the constructed configurations, the conformation with the lowest energy was selected to minimize energy and optimize the lattice model. In this model, the Discover module was used to simulate NVT dynamics at 298 K; subsequently, 2.0 ns was required to analyze the cohesive energy density of the system, followed by 2.0 ns to simulate NVT dynamics to stabilize the density of the system. Finally, the equilibrium system was simulated using 2.0 ns full-trajectory dynamics and the simulation step was set at 0.5 fs. In the simulations, the Andersen method was used to control pressure and the Berendsen method was used to control temperature. The cutoff radius was 0.5 nm, the parameters of the nonbond method and Coulomb interaction were set as Vdw and Coulomb, respectively, and a group-based method was used to calculate the nonbonding force. The diffusion coefficients (D) were calculated using the Einstein relation[56,57] as follows

$$D = \frac{1}{6N} \lim_{t \to \infty} \frac{d}{dt} \sum_{i=1}^{N} \langle |r_i(t) - r_i(0)|^2 \rangle \tag{7}$$

where $r_i(t)$ is the position of the ith molecule or ion at time t and N is the number of molecules or ions.

Simulation of Diffusion for a Mixture of Mg^{2+} and $[Fe(CN)_6]^{3-}$. To evaluate the diffusion of a mixture of Mg^{2+} and $[Fe(CN)_6]^{3-}$ in water through the membrane (along the z direction), the ion-flux profile (number of ions passing through the membrane with respect to simulation time) was calculated. The equilibrated membrane system was placed in the middle of the simulation box, and a periodic-boundary condition was applied in the x–y direction. A mixture of Mg^{2+} ions, $[Fe(CN)_6]^{3-}$ ions, and H_2O molecules (16, 16, and more than 5500, respectively) was placed on the left of the membrane along the z direction, whereas on the right, only H_2O molecules existed. Subsequently, the NPT dynamics were simulated at 298 K. The Andersen method was used to control pressure, while the Berendsen method was used to control temperature; the parameters of the nonbond method and Coulomb interaction were set as Vdw and Coulomb, respectively. Images corresponding to diffusion simulations at 50 and 200 ns were produced using VMD software.[58]

ASSOCIATED CONTENT

Ⓢ Supporting Information

The Supporting Information is available free of charge at https://pubs.acs.org/doi/10.1021/acsnano.1c03194.

Structure of TCB monomer and the optimized elementary pore structure of the polymerized film; structural and chemical characterization, pure water

permeance of CNT porous support (SEM and AFM images, Raman spectra, XPS spectra, zeta potential, pore size); additional structural characterization of CMP membranes (SEM, AFM, and TEM images, the peak force quantitative nanomechanical mapping curve, surface zeta potential); performance of the CMP membranes and Nafion 211 membrane; schematic illustrations of the membrane adsorption test setup and pressure-driven cross-flow permeation system; membrane adsorption test results; list of analyzed species and their ionic and hydrated radii (PDF)

AUTHOR INFORMATION

Corresponding Author

Zhiping Lai − *Division of Physical Science and Engineering, King Abdullah University of Science and Technology (KAUST), Thuwal 23955-6900, Saudi Arabia*; ⓞ orcid.org/0000-0001-9555-6009; Email: zhiping.lai@kaust.edu.sa

Authors

Zongyao Zhou − *Division of Physical Science and Engineering, King Abdullah University of Science and Technology (KAUST), Thuwal 23955-6900, Saudi Arabia*; ⓞ orcid.org/0000-0002-4694-2330

Dong Guo − *Division of Physical Science and Engineering, King Abdullah University of Science and Technology (KAUST), Thuwal 23955-6900, Saudi Arabia*; ⓞ orcid.org/0000-0002-1055-482X

Digambar B. Shinde − *Division of Physical Science and Engineering, King Abdullah University of Science and Technology (KAUST), Thuwal 23955-6900, Saudi Arabia*

Li Cao − *Division of Physical Science and Engineering, King Abdullah University of Science and Technology (KAUST), Thuwal 23955-6900, Saudi Arabia*

Zhen Li − *Division of Physical Science and Engineering, King Abdullah University of Science and Technology (KAUST), Thuwal 23955-6900, Saudi Arabia*

Xiang Li − *Division of Physical Science and Engineering, King Abdullah University of Science and Technology (KAUST), Thuwal 23955-6900, Saudi Arabia*; ⓞ orcid.org/0000-0002-5656-1363

Dongwei Lu − *Division of Physical Science and Engineering, King Abdullah University of Science and Technology (KAUST), Thuwal 23955-6900, Saudi Arabia*

Complete contact information is available at:
https://pubs.acs.org/10.1021/acsnano.1c03194

Notes

The authors declare no competing financial interest.

REFERENCES

(1) Mi, B. Graphene Oxide Membranes for Ionic and Molecular Sieving. *Science* **2014**, *343* (6172), 740−742.

(2) Shannon, M. A.; Bohn, P. W.; Elimelech, M.; Georgiadis, J. G.; Marinas, B. J.; Mayes, A. M. Science and Technology for Water Purification in the Coming Decades. In *Nanoscience and Technology: A*

Collection of Reviews from Nature Journals; World Scientific, 2010; pp 337−346.

(3) Gin, D. L.; Noble, R. D. Designing the Next Generation of Chemical Separation Membranes. *Science* **2011**, *332* (6030), 674−676.

(4) Werber, J. R.; Elimelech, M. Permselectivity Limits of Biomimetic Desalination Membranes. *Science advances* **2018**, *4* (6), No. eaar8266.

(5) Lu, P.; Min, D.; DiMaio, F.; Wei, K. Y.; Vahey, M. D.; Boyken, S. E.; Chen, Z.; Fallas, J. A.; Ueda, G.; Sheffler, W.; et al. Accurate Computational Design of Multipass Transmembrane Proteins. *Science* **2018**, *359* (6379), 1042−1046.

(6) Doyle, D. A.; Cabral, J. M.; Pfuetzner, R. A.; Kuo, A.; Gulbis, J. M.; Cohen, S. L.; Chait, B. T.; MacKinnon, R. The Structure of the Potassium Channel: Molecular Basis of K$^+$ Conduction and Selectivity. *Science* **1998**, *280* (5360), 69−77.

(7) Liang, Y.; Zhu, Y.; Liu, C.; Lee, K.-R; Hung, W.-S.; Wang, Z.; Li, Y.; Elimelech, M.; Jin, J.; Lin, S. Polyamide Nanofiltration Membrane with Highly Uniform Sub-Nanometre Pores for Sub-1 Å Precision Separation. *Nat. Commun.* **2020**, *11* (1), 2015.

(8) Dai, Q.; Lu, W.; Zhao, Y.; Zhang, H.; Zhu, X.; Li, X. Advanced Scalable Zeolite "Ions-Sieving" Composite Membranes with High Selectivity. *J. Membr. Sci.* **2020**, *595*, 117569.

(9) Dong, J.; Xu, Z.; Yang, S.; Murad, S.; Hinkle, K. R. Zeolite Membranes for Ion Separations from Aqueous Solutions. *Curr. Opin. Chem. Eng.* **2015**, *8*, 15−20.

(10) Yuan, Z.; Zhu, X.; Li, M.; Lu, W.; Li, X.; Zhang, H. A Highly Ion-Selective Zeolite Flake Layer on Porous Membranes for Flow Battery Applications. *Angew. Chem.* **2016**, *128* (9), 3110−3114.

(11) Peng, Y.; Li, Y.; Ban, Y.; Jin, H.; Jiao, W.; Liu, X.; Yang, W. Metal-Organic Framework Nanosheets as Building Blocks for Molecular Sieving Membranes. *Science* **2014**, *346* (6215), 1356−1359.

(12) Li, W.; Zhang, Y.; Zhang, C.; Meng, Q.; Xu, Z.; Su, P.; Li, Q.; Shen, C.; Fan, Z.; Qin, L.; Zhang, G. Transformation of Metal-Organic Frameworks for Molecular Sieving Membranes. *Nat. Commun.* **2016**, *7* (1), 11315.

(13) Lu, J.; Zhang, H.; Hou, J.; Li, X.; Hu, X.; Hu, Y.; Easton, C. D.; Li, Q.; Sun, C.; Thornton, A. W.; et al. Efficient Metal Ion Sieving in Rectifying Subnanochannels Enabled by Metal−Organic Frameworks. *Nat. Mater.* **2020**, *19*, 767−774.

(14) Zhang, H.; Hou, J.; Hu, Y.; Wang, P.; Ou, R.; Jiang, L.; Liu, J. Z.; Freeman, B. D.; Hill, A. J.; Wang, H. Ultrafast Selective Transport of Alkali Metal Ions in Metal Organic Frameworks with Subnanometer Pores. *Sci. Adv.* **2018**, *4* (2), No. eaaq0066.

(15) Zhang, W.; Zhang, L.; Zhao, H.; Li, B.; Ma, H. A Two-Dimensional Cationic Covalent Organic Framework Membrane for Selective Molecular Sieving. *J. Mater. Chem. A* **2018**, *6* (27), 13331−13339.

(16) Jiang, C.; Tang, M.; Zhu, S.; Zhang, J.; Wu, Y.; Chen, Y.; Xia, C.; Wang, C.; Hu, W. Constructing Universal Ionic Sieves *via* Alignment of Two-Dimensional Covalent Organic Frameworks (Cofs). *Angew. Chem.* **2018**, *130* (49), 16304−16308.

(17) Li, Y.; Wu, Q.; Guo, X.; Zhang, M.; Chen, B.; Wei, G.; Li, X.; Li, X.; Li, S.; Ma, L. Laminated Self-Standing Covalent Organic Framework Membrane with Uniformly Distributed Subnanopores for Ionic and Molecular Sieving. *Nat. Commun.* **2020**, *11* (1), 599.

(18) Joshi, R.; Carbone, P.; Wang, F.-C.; Kravets, V. G.; Su, Y.; Grigorieva, I. V.; Wu, H.; Geim, A. K.; Nair, R. R. Precise and Ultrafast Molecular Sieving through Graphene Oxide Membranes. *Science* **2014**, *343* (6172), 752−754.

(19) Abraham, J.; Vasu, K. S.; Williams, C. D.; Gopinadhan, K.; Su, Y.; Cherian, C. T.; Dix, J.; Prestat, E.; Haigh, S. J.; Grigorieva, I. V.; et al. Tunable Sieving of Ions Using Graphene Oxide Membranes. *Nat. Nanotechnol.* **2017**, *12* (6), 546.

(20) Yang, Q.; Su, Y.; Chi, C.; Cherian, C.; Huang, K.; Kravets, V.; Wang, F.; Zhang, J.; Pratt, A.; Grigorenko, A.; et al. Ultrathin Graphene-Based Membrane with Precise Molecular Sieving and Ultrafast Solvent Permeation. *Nat. Mater.* **2017**, *16* (12), 1198−1202.

(21) Li, H.; Song, Z.; Zhang, X.; Huang, Y.; Li, S.; Mao, Y.; Ploehn, H. J.; Bao, Y.; Yu, M. Ultrathin, Molecular-Sieving Graphene Oxide Membranes for Selective Hydrogen Separation. *Science* **2013**, *342* (6154), 95−98.

(22) Qi, B.; He, X.; Zeng, G.; Pan, Y.; Li, G.; Liu, G.; Zhang, Y.; Chen, W.; Sun, Y. Strict Molecular Sieving over Electrodeposited 2D-Interspacing-Narrowed Graphene Oxide Membranes. *Nat. Commun.* **2017**, *8* (1), 825.

(23) Park, H. B.; Jung, C. H.; Lee, Y. M.; Hill, A. J.; Pas, S. J.; Mudie, S. T.; Van Wagner, E.; Freeman, B. D.; Cookson, D. J. Polymers with Cavities Tuned for Fast Selective Transport of Small Molecules and Ions. *Science* **2007**, *318* (5848), 254−258.

(24) Cheng, X. Q.; Wang, Z. X.; Jiang, X.; Li, T.; Lau, C. H.; Guo, Z.; Ma, J.; Shao, L. Towards Sustainable Ultrafast Molecular-Separation Membranes: From Conventional Polymers to Emerging Materials. *Prog. Mater. Sci.* **2018**, *92*, 258−283.

(25) Lee, J.-S. M.; Cooper, A. I. Advances in Conjugated Microporous Polymers. *Chem. Rev.* **2020**, *120* (4), 2171−2214.

(26) Jiang, J.-X.; Su, F.; Trewin, A.; Wood, C. D.; Campbell, N. L.; Niu, H.; Dickinson, C.; Ganin, A. Y.; Rosseinsky, M. J.; Khimyak, Y. Z.; Cooper, A. I. Conjugated Microporous Poly (aryleneethynylene) Networks. *Angew. Chem., Int. Ed.* **2007**, *46* (45), 8574−8578.

(27) Wang, S.; Zhang, C.; Shu, Y.; Jiang, S.; Xia, Q.; Chen, L.; Jin, S.; Hussain, I.; Cooper, A. I.; Tan, B. Layered Microporous Polymers by Solvent Knitting Method. *Sci. Adv.* **2017**, *3* (3), No. e1602610.

(28) Zhou, Z.; Li, X.; Guo, D.; Shinde, D. B.; Lu, D.; Chen, L.; Liu, X.; Cao, L.; Aboalsaud, A. M.; Hu, Y.; Lai, Z. Electropolymerization of Robust Conjugated Microporous Polymer Membranes for Rapid Solvent Transport and Narrow Molecular Sieving. *Nat. Commun.* **2020**, *11* (1), 5323.

(29) Zhou, Z.; Hu, Y.; Wang, Q.; Mi, B. Carbon Nanotube-Supported Polyamide Membrane with Minimized Internal Concentration Polarization for Both Aqueous and Organic Solvent Forward Osmosis Process. *J. Membr. Sci.* **2020**, *611*, 118273.

(30) Suresh, V. M.; Scherf, U. Electrochemically Generated Conjugated Microporous Polymer Network Thin Films for Chemical Sensor Applications. *Macromol. Chem. Phys.* **2018**, *219* (18), 1800207.

(31) Gu, C.; Zhang, Z.; Sun, S.; Pan, Y.; Zhong, C.; Lv, Y.; Li, M.; Ariga, K.; Huang, F.; Ma, Y. *In Situ* Electrochemical Deposition and Doping of C60 Films Applied to High-Performance Inverted Organic Photovoltaics. *Adv. Mater.* **2012**, *24* (42), 5727−5731.

(32) Guo, D.; Li, X.; Wahyudi, W.; Li, C.; Emwas, A.-H.; Hedhili, M. N.; Li, Y.; Lai, Z. Electropolymerized Conjugated Microporous Nanoskin Regulating Polysulfide and Electrolyte for High-Energy Li−S Batteries. *ACS Nano* **2020**, *14* (12), 17163−17173.

(33) Shinde, D. B.; Sheng, G.; Li, X.; Ostwal, M.; Emwas, A.-H.; Huang, K.-W.; Lai, Z. Crystalline 2D Covalent Organic Framework Membranes for High-Flux Organic Solvent Nanofiltration. *J. Am. Chem. Soc.* **2018**, *140* (43), 14342−14349.

(34) Dey, K. P.; Kundu, D.; Chatterjee, M.; Naskar, M. K. Preparation of Naa Zeolite Membranes Using Poly(ethyleneimine) as Buffer Layer, and Study of Their Permeation Behavior. *J. Am. Ceram. Soc.* **2013**, *96* (1), 68−72.

(35) Bae, Y.-S.; Yazaydın, A. O.; Snurr, R. Q. Evaluation of the Bet Method for Determining Surface Areas of Mofs and Zeolites That Contain Ultra-Micropores. *Langmuir* **2010**, *26* (8), 5475−5483.

(36) Furukawa, H.; Ko, N.; Go, Y. B.; Aratani, N.; Choi, S. B.; Choi, E.; Yazaydin, A. O.; Snurr, R. Q.; O'Keeffe, M.; Kim, J.; Yaghi, O. M. Ultrahigh Porosity in Metal-Organic Frameworks. *Science* **2010**, *329* (5990), 424−428.

(37) Liang, B.; Wang, H.; Shi, X.; Shen, B.; He, X.; Ghazi, Z. A.; Khan, N. A.; Sin, H.; Khattak, A. M.; Li, L.; Tang, Z. Microporous Membranes Comprising Conjugated Polymers with Rigid Backbones Enable Ultrafast Organic-Solvent Nanofiltration. *Nat. Chem.* **2018**, *10* (9), 961−967.

(38) Tan, R.; Wang, A.; Malpass-Evans, R.; Williams, R.; Zhao, E. W.; Liu, T.; Ye, C.; Zhou, X.; Darwich, B. P.; Fan, Z.; et al. Hydrophilic Microporous Membranes for Selective Ion Separation and Flow-Battery Energy Storage. *Nat. Mater.* **2020**, *19* (2), 195−202.

(39) Ren, C. E.; Hatzell, K. B.; Alhabeb, M.; Ling, Z.; Mahmoud, K. A.; Gogotsi, Y. Charge-and Size-Selective Ion Sieving through Ti3c2t X Mxene Membranes. *J. Phys. Chem. Lett.* **2015**, *6* (20), 4026−4031.

(40) Xi, Y.-H.; Liu, Z.; Ji, J.; Wang, Y.; Faraj, Y.; Zhu, Y.; Xie, R.; Ju, X.-J.; Wang, W.; Lu, X.; Chu, L.-Y. Graphene-Based Membranes with Uniform 2D Nanochannels for Precise Sieving of Mono-/Multi-Valent Metal Ions. *J. Membr. Sci.* **2018**, *550*, 208−218.

(41) Zhu, J.; Wang, L.; Wang, J.; Wang, F.; Tian, M.; Zheng, S.; Shao, N.; Wang, L.; He, M. Precisely Tunable Ion Sieving with an Al13−Ti3c2t X Lamellar Membrane by Controlling Interlayer Spacing. *ACS Nano* **2020**, *14* (11), 15306−15316.

(42) Wang, J.; Zhang, Z.; Zhu, J.; Tian, M.; Zheng, S.; Wang, F.; Wang, X.; Wang, L. Ion Sieving by a Two-Dimensional Ti 3 C 2 T X Alginate Lamellar Membrane with Stable Interlayer Spacing. *Nat. Commun.* **2020**, *11* (1), 3540.

(43) Esfandiar, A.; Radha, B.; Wang, F.; Yang, Q.; Hu, S.; Garaj, S.; Nair, R.; Geim, A.; Gopinadhan, K. Size Effect in Ion Transport through Angstrom-Scale Slits. *Science* **2017**, *358* (6362), 511−513.

(44) Gong, G.; Wang, P.; Zhou, Z.; Hu, Y. New Insights into the Role of an Interlayer for the Fabrication of Highly Selective and Permeable Thin-Film Composite Nanofiltration Membrane. *ACS Appl. Mater. Interfaces* **2019**, *11* (7), 7349−7356.

(45) Hatakeyama, E. S.; Gabriel, C. J.; Wiesenauer, B. R.; Lohr, J. L.; Zhou, M.; Noble, R. D.; Gin, D. L. Water Filtration Performance of a Lyotropic Liquid Crystal Polymer Membrane with Uniform, Sub-1-Nm Pores. *J. Membr. Sci.* **2011**, *366* (1−2), 62−72.

(46) Lu, T. *Multiwfn: A Multifunctional Wavefunction Analyzer*, ver. 3.3.3; Beijing Kein Research Center for Natural Sciences: Beijing, China, 2014.

(47) Willems, T. F.; Rycroft, C. H.; Kazi, M.; Meza, J. C.; Haranczyk, M. Algorithms and Tools for High-Throughput Geometry-Based Analysis of Crystalline Porous Materials. *Microporous Mesoporous Mater.* **2012**, *149* (1), 134−141.

(48) Gu, C.; Chen, Y.; Zhang, Z.; Xue, S.; Sun, S.; Zhang, K.; Zhong, C.; Zhang, H.; Pan, Y.; Lv, Y.; et al. Electrochemical Route to Fabricate Film-Like Conjugated Microporous Polymers and Application for Organic Electronics. *Adv. Mater.* **2013**, *25* (25), 3443−3448.

(49) Desbene-Monvernay, A.; Lacaze, P.; Delamar, M. A Quantitative Study of Cross-Linking in Electrodeposited Carbazole Films Using Tetrabutylammonium Tribromide Bromination and XPS Analysis. *J. Electroanal. Chem.* **1992**, *334* (1−2), 241−246.

(50) Desbene-Monvernay, A.; Lacaze, P.-C.; Dubois, J.-E. Polaromicrotribometric (Pmt) and Ir, Esca, Epr Spectroscopic Study of Colored Radical Films Formed by the Electrochemical Oxidation of Carbazoles: Part I. Carbazole and N-Ethyl, N-Phenyl and N-Carbazyl Derivatives. *J. Electroanal. Chem. Interfacial Electrochem.* **1981**, *129* (1−2), 229−241.

(51) Frisch, M. J.; Trucks, G. W.; Schlegel, H. B.; Scuseria, G. E.; Robb, M. A.; Cheeseman, J. R.; Scalmani, G.; Barone, V.; Mennucci, B.; Petersson, G. A.; Nakatsuji, H.; Caricato, M.; Li, X.; Hratchian, H. P.; Izmaylov, A. F.; Bloino, J.; Zheng, G.; Sonnenberg, J. L.; Hada, M.; Ehara, M.; et al. *Gaussian 09*, Rev. B.01; Gaussian, Inc.: Wallingford, CT, 2010.

(52) Murray, J. S.; Politzer, P. The Electrostatic Potential: An Overview. *Wiley Interdiscip. Rev.: Comput. Mol. Sci.* **2011**, *1* (2), 153−163.

(53) Hess, B.; Kutzner, C.; Van Der Spoel, D.; Lindahl, E. Gromacs 4: Algorithms for Highly Efficient, Load-Balanced, and Scalable Molecular Simulation. *J. Chem. Theory Comput.* **2008**, *4* (3), 435−447.

(54) Oostenbrink, C.; Villa, A.; Mark, A. E.; Van Gunsteren, W. F. A Biomolecular Force Field Based on the Free Enthalpy of Hydration and Solvation: The Gromos Force-Field Parameter Sets 53a5 and 53a6. *J. Comput. Chem.* **2004**, *25* (13), 1656−1676.

(55) Schüttelkopf, A. W.; Van Aalten, D. M. Prodrg: A Tool for High-Throughput Crystallography of Protein−Ligand Complexes. *Acta Crystallogr., Sect. D: Biol. Crystallogr.* **2004**, *60* (8), 1355−1363.

(56) Coelho, L.; De Oliveira, J.; Tavares, F.; Matthews, M. A. Role of Attractive Forces in Self-Diffusion and Mutual Diffusion in Dense Simple Fluids and Real Substances. *Fluid Phase Equilib.* **2002**, *194*, 1131−1140.

(57) Peters, J. Einstein's Relation. *Eur. J. Phys.* **1982**, *3* (1), 19.

(58) Humphrey, W.; Dalke, A.; Schulten, K. VMD: Visual Molecular Dynamics. *J. Mol. Graphics* **1996**, *14* (1), 33−38.